



The Oxidation of the HiSiMo Cast Irons Alloyed with Cr/Al at 800 °C

Wenhui Zhu¹ · Bruce A. Pint² · Yang Huo¹ · Larry Godlewski¹ · Bitra Ghaffari¹ · Simon Lekakh³ · Carlos Engler-Pinto¹ · Mei Li¹

Received: 19 November 2021 / Revised: 4 January 2022 / Accepted: 5 January 2022 /
Published online: 4 March 2022

© Ford Motor Company, under exclusive licence to Springer Science+Business Media LLC, part of Springer Nature 2022

Abstract

To improve the oxidation resistance of cast iron containing Si and Mo (HiSiMo), 1wt.% Cr and 3wt.% Al were added into the base alloy to improve high temperature oxidation resistance for exhaust manifold applications. Oxidation tests were performed in both dry and wet air (air+10% H₂O) at 800 °C for 1, 10, 24, and 50 h. The mass change and oxide thickness were measured to evaluate the oxidation resistance. Scanning electron microscopy with energy dispersive X-ray spectroscopy (SEM/EDS) and transmission electron microscopy (TEM) were employed to characterize the oxidized samples. The results showed that the additions of Al or Cr selectively oxidized to form a more oxidation resistant surface oxide layer, which reduced the mass gain during these experiments.

Keywords HiSiMo · Cast iron · Oxidation · TEM

Introduction

Spheroidal graphite cast irons have been widely used in automotive parts such as brake discs and brake drums, engine heads, diesel engine blocks, heat exchangers, and exhaust manifolds because of their good thermal conductivity, high strength, excellent fatigue resistance and low cost [1–3]. HiSiMo cast irons are one of the most extensively used alloys for exhaust manifolds up to ~800 °C based on their high-temperature oxidation and thermal fatigue resistance [4–10]. In recent years,

✉ Wenhui Zhu
wzhu45@ford.com

¹ Research and Innovation Center, Ford Motor Company, Dearborn, MI 48124, USA

² Materials Science and Technology Division, Oak Ridge National Laboratory, Oak Ridge, TN 37831-6156, USA

³ Missouri University of Science and Technology, Rolla, MO 65409, USA

the maximum combustion temperature has increased to almost 900 °C due to the high demand for increased fuel economy [11–13]. To improve the performance of HiSiMo cast irons [4, 14, 15], different alloying strategies have been developed, such as Cr and Al additions [8, 16]. Among the alloys studied, additions of 1wt.% Cr and 3wt.% Al were the most effective to enhance thermomechanical fatigue performance under high temperature oxidation conditions. In this study, oxidation results for these Cr and Al additions are presented at 800 °C.

Experimental

Three cast irons were studied in this work: the base HiSiMo (HSM) cast iron, HiSiMo with 1wt.% Cr (HSM1Cr) and 3wt.% Al (HSM3Al). Their chemical compositions are listed in Table 1. The casting and sampling was done at Missouri University of Science and Technology, and the details have been reported previously [16]. The oxidation experiments were conducted at Oak Ridge National Laboratory (ORNL) in controlled environments to simulate oxidation under service conditions. The 20×10×1.5 mm samples were oxidized in automated cyclic oxidation rigs [17] with 6 min (0.1 h) per cycle in the resistively heated tube furnace at 800±2 °C and 10 min cooling between cycles for 10, 100, 240 or 500 cycles or 1, 10, 24, and 50 h. The oxidation environments were; (1) dry air, and (2) “wet” air, which is air with 10±1 vol.% H₂O to simulate a combustion environment [18]. The water was added by atomization into the flowing air (850 cc/min). The specimen mass change was monitored before and after oxidation using a Mettler Toledo XP205 balance with an accuracy of ±0.04 mg or ~0.01 mg/cm². The oxide thicknesses were measured using image analysis of optical microscopy of polished cross-sections with typically 30 measurements made on three images. The specimens for TEM analysis were prepared using focused ion beam (FIB) on a Thermo Fisher Helios 650 Nanolab SEM/FIB. The Scanning TEM (STEM) imaging was carried out using a Thermo Fisher Talos F200X STEM operated at 200 kV and equipped with an integrated energy dispersive X-ray spectrometer (EDS) with four silicon drift detectors.

Results and Discussion

The measured mass change of the three alloys during and after oxidation to characterize the oxidation resistance at 800 °C, as shown in Fig. 1. Figure 1a shows the final mass change for specimens stopped after tests for 1–50 h in dry and wet air.

Table 1 Chemical compositions, in wt.%, of the cast irons studied in this work

Alloy	Fe	Si	Mo	C	Cr	Al	Ni	Mn	Mg	Ce	Hf	La	S
HSM	91.3	4.1	0.8	3.2	0.07	0.01	0.2	0.3	0.02	0.01	0.003	0.007	0.006
HSM1Cr	89.5	4.8	0.8	2.9	1.1	0.02	0.3	0.3	0.04	0.03	0.003	0.009	0.003
HSM3Al	88.8	3.1	0.8	2.7	0.08	3.5	0.6	0.1	0.04	0.03	0.002	0.009	0.003

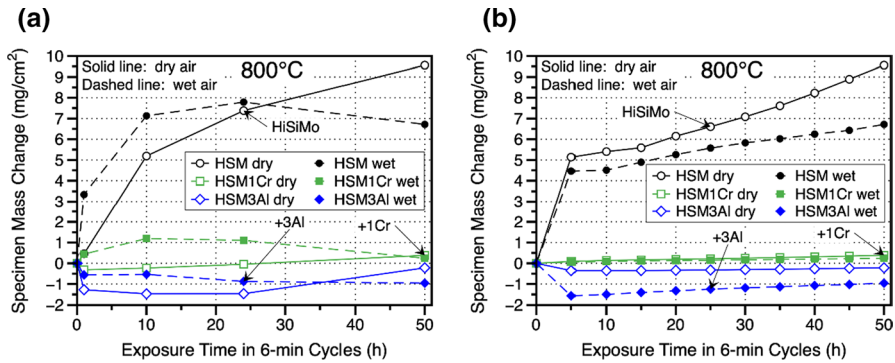


Fig. 1 Mass change with time of the three alloys after oxidation at 800 °C in dry and wet air using 6-min cycles, **a** final mass change for four different specimens of each alloy stopped at different times, **b** mass change for the set of specimens exposed for 50 h

Figure 1b shows the mass change during exposures for 50 h where the specimen was stopped and weighed every 50 cycles (5 h of total exposure). In Fig. 1a, a mass gain was observed for all of the baseline HSM specimens. Especially for the HSM3Al specimens, mass losses were consistently measured because of C loss as the large graphite nodules near the surface were oxidized [10]. The HSM3Al mass losses suggest that C loss dominated over O uptake associated with oxide formation under these conditions. In Fig. 1b, the HSM3Al specimen showed a consistent mass gain after the initial mass loss after 5 h in wet air. Compared to the HSM mass gains, this suggests that the mass gain due to oxide formation was much higher for the baseline HSM specimens compared to those alloyed with Al or Cr. For the HSM1Cr specimens, the specimens exposed for short times in dry air showed mass losses but all HSM1Cr specimens exposed in wet air showed mass gains. Accelerated oxide growth with the addition of H₂O is typical [7]. For the HSM baseline specimens, the lower mass gain after 50 h in wet air suggests that scale spallation may have occurred.

Figure 2 shows oxide thickness measurements for all of the specimens in Fig. 1a. For some of the data sets, box and whisker plots are shown to visualize the data sets. The whiskers not the maximum and minimum values measured and the boxes are defined by the 25 and 75% values with the median values marked in the box. As the distributions were not normal, the lines in Fig. 2 link the median values in dry and wet air. Consistent with the mass change data, the values were much lower for the HSM1Cr and HSM3Al specimens in both environments. Because the HSM1Cr and HSM3Al specimens all formed oxides of similar thickness, boxes are only shown for the wet air exposures. Compared to the baseline HSM specimens, there was roughly an order of magnitude reduction in oxide thickness with the Cr and Al additions. The 3wt.% Al alloying reduced the scale thickness by ~90% in both environments and the 1wt.% Cr alloying reduced it by ~86% in both conditions.

Figure 3 shows SEM images of the samples after cyclic oxidation at 800 °C for 50 h in dry and wet air. Figure 3a and b are the SEM/EDS of HSM in wet and dry air, respectively. Consistent with Fig. 2, the oxide layer in wet air was slightly

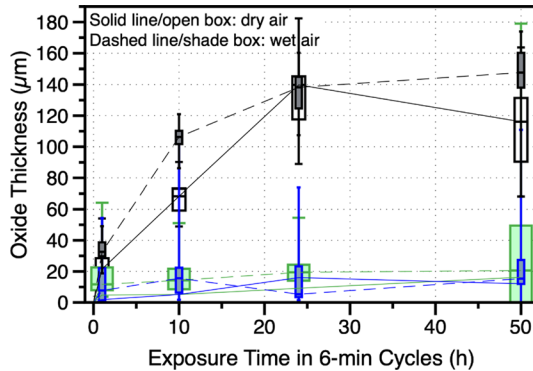


Fig. 2 Oxide thickness change of the three different alloys with time in dry and wet air conditions. The lines connect the median values. The boxes are defined by the 25 and 75% values and the whiskers are the minimum and maximum values measured. The shaded boxes and dashed lines are for wet air experiments and the open boxes and solid lines designate dry air conditions. The colors are adopted from Fig. 1, The black-and-white is HSM, blue HSM3Al, green HSM1Cr

thicker than that in dry air. A typical duplex structure was observed for the Fe-rich oxide as has been observed previously [7, 8, 19] with the inner layer growing by inward transport and the outer layer by outward Fe diffusion. Because there was no Cr or Al added in this alloy, the oxidation resistance of HSM was mainly affected by the Si addition and Si enrichment was detected in the inner oxide layer in both specimens.

Compared to the base HSM, HSM1Cr, and HSM3Al showed improved oxidation resistance, which is more evident in Fig. 3d and e, than in Fig. 3c and f. The thick duplex oxide developed from nucleated islands and then expanded across the surface. The SEM images only show a small region of the surface whereas the oxide thickness measurements in Fig. 2 cover a larger area and are more representative of the overall oxidation behavior. For the HSM1Cr specimens in Fig. 3c and d, the Cr addition resulted in a Cr-rich oxide layer that slowed the diffusion of oxygen, resulting in oxide layers that were much thinner compared to those formed on the HSM specimens. For the HSM3Al specimens in Fig. 3e and f, an Al-rich oxide layer is evident in the EDS maps, which appeared to significantly improve oxidation resistance. In some regions, the oxide was much thinner, such as Fig. 3d and e.

Because of the thin Cr- and Al-rich oxide layers in Fig. 3, TEM of the HSM1Cr and HSM3Al specimens were conducted to further investigate the microstructure of the reaction products. Figure 4 shows the STEM/EDS mapping of the HSM1Cr specimen exposed in wet air at 800 °C for 50 h. The Cr-rich oxides were layered among the Fe- and Mn-rich oxides.

The Cr-rich oxide layer adjacent to the substrate was above the last Si-rich oxide layer, which is consistent with the Ellingham diagram [20]. These layered oxides suggest that the Cr-rich oxide layers formed but then were not stable because of the low Cr content. Similar structures have been observed before for low alloy steels [21–23]. The oxidation in dry air was similar. Figure 5 shows a region where only one Cr-rich inner layer formed with an Si-rich layer beneath. The thicker outer oxide

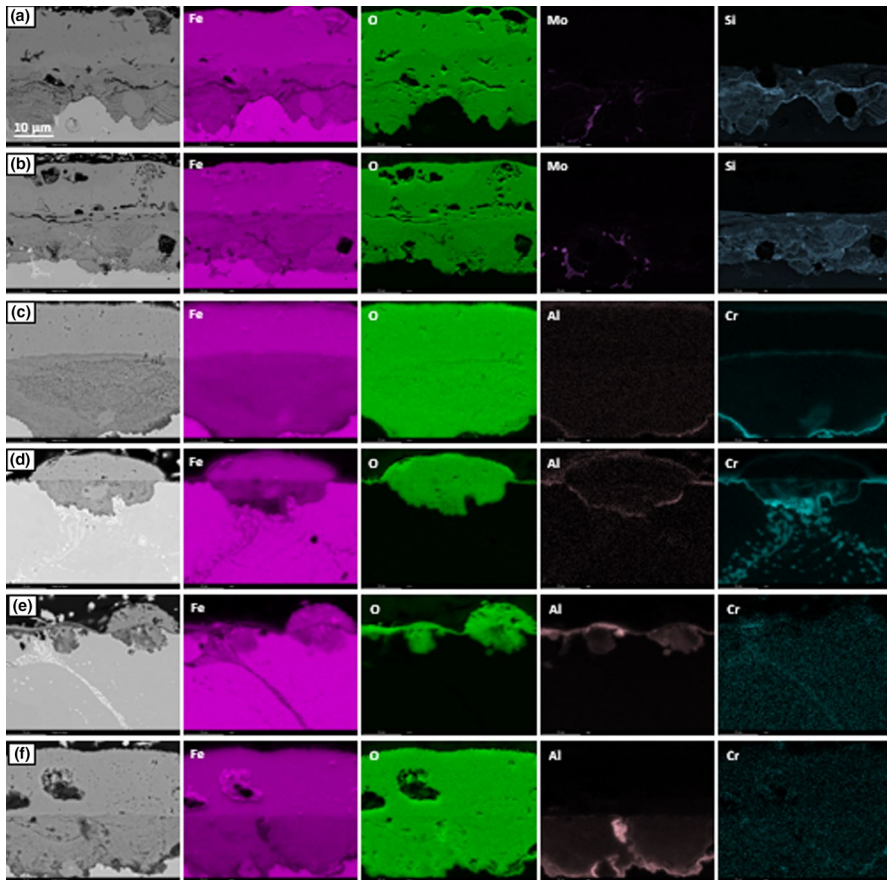


Fig. 3 SEM images of the alloys after oxidation at 800 °C for 50 h. **a** HSM in wet air, **b** HSM in dry air, **c** HSM1Cr in wet air, **d** HSM1Cr in dry air, **e** HSM3Al in wet air, **f** HSM3Al in dry air. The scale in all images is the same, as shown by the 10 μm bar in (**a**)

layer was rich in Fe and Mn. Mn is a fast diffusing, oxygen-active element that often becomes enriched in thermally grown scales [18, 24, 25]. Figure 6a is a HRTEM image of the interface region between the substrate and scale. The substrate was shown and marked on the right-hand side of the image. Adjacent to the substrate is the Si-rich oxide layer, which is amorphous according to the fast Fourier transformation (FFT) shown in Fig. 6c. If continuous, this amorphous layer can help inhibit the diffusion of oxygen and perhaps is more effective because there are no grain boundaries like those observed in the adjacent crystalline oxide layers. The crystal structure of the Cr- and Mn-rich oxide layers were identified in Fig. 6b and d, with the Cr-rich oxide layer right above the Si-rich oxide layer and the Mn-rich oxide above the Cr-rich oxide.

As for the HSM3Al specimens, the oxidation mechanism was similar to that of HSM1Cr, but Al_2O_3 is more thermodynamically stable than SiO_2 [5] so a Si-rich

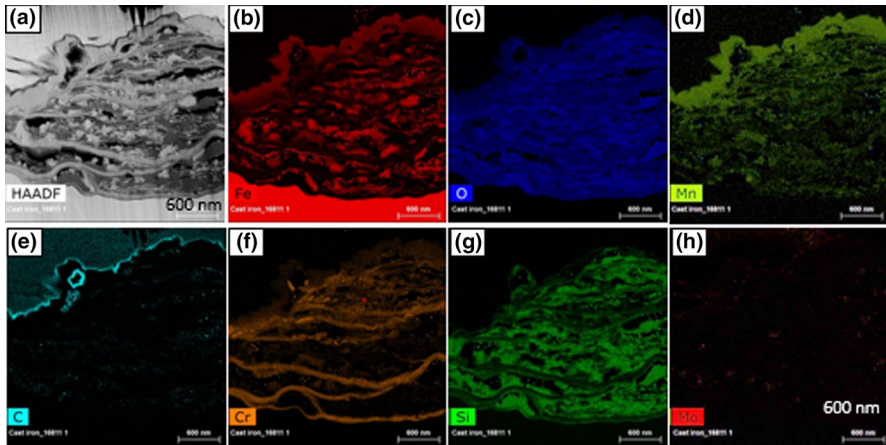


Fig. 4 STEM/EDS mapping of HSM1Cr alloy oxidized in wet air at 800 °C for 50 h. The scale bar is 600 nm

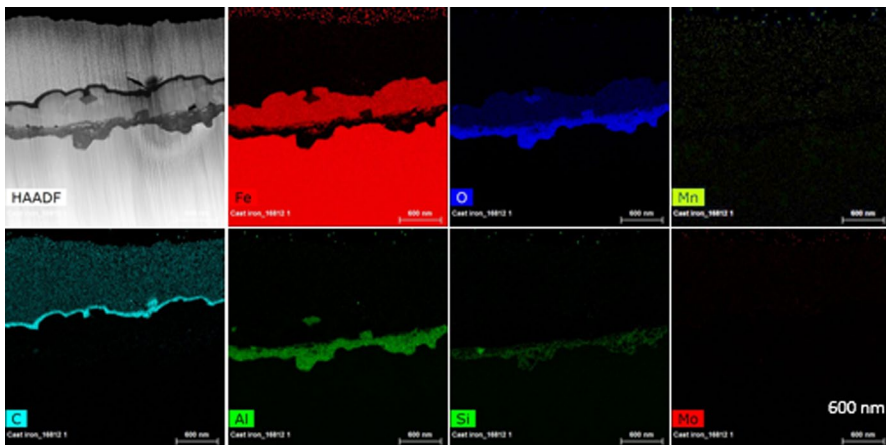


Fig. 5 STEM/EDS mapping of HSM1Cr alloy oxidized in dry air at 800 °C for 50 h. The large bright area in (a) was the Pt layer deposited during TEM specimen preparation by Focused Ion Beam. The scale bar is 600 nm

sub-layer was not observed. Figures 7 and 8 display the STEM/EDS mapping of HSM3Al specimens exposed in wet and dry air, respectively. The addition of Al introduced an Al-rich oxide layer besides Fe- and Si-rich oxide layers. The formation of the Al-rich layer improved the oxidation resistance. Since Figs. 7 and 8 only show a small region of the samples, they were not representative of the average thickness of the oxide layer formed on these specimens. The SEM/EDS mapping in Fig. 3e and f, which imaged a substantially larger area, showed a more representative region with the oxide thickness varying due to the fact that the oxidation started from multiple islands and then spread out more fully on the substrate surface.

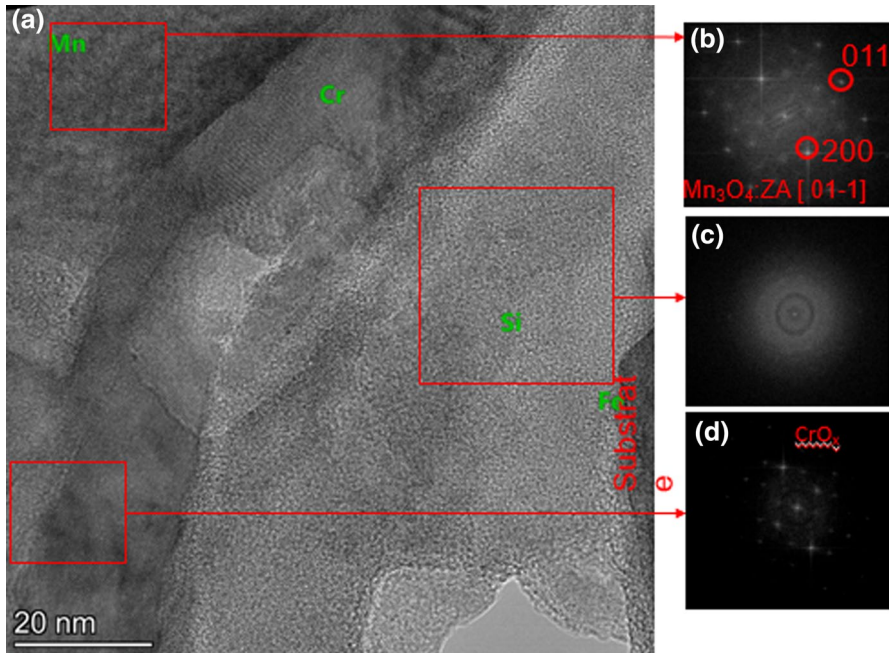


Fig. 6 The HRTEM image of the layered structure of the oxides right above the HSM1Cr substrate after oxidation in dry air

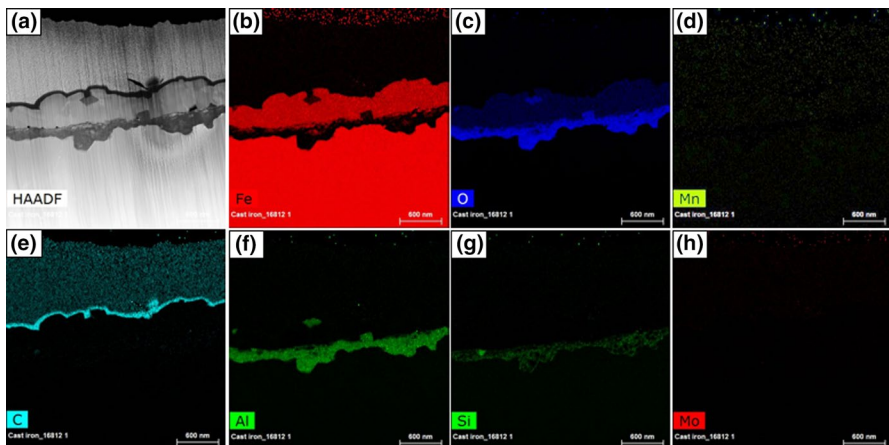


Fig. 7 STEM/EDS mapping of HSM3Al alloy oxidized in wet air at 800 °C for 50 h

With the introduction of Al, an extra oxide layer of aluminum/chrome oxide with traces of iron and Si formed. Next to this layer was a layer of silicide formed because of the depletion by aluminum. This provided a secondary oxidation protection [26, 27]. For the alloys with Cr introduction, the oxidation at high temperature led to either chrome oxides formation accompanied by the subsurface carbide dissolution

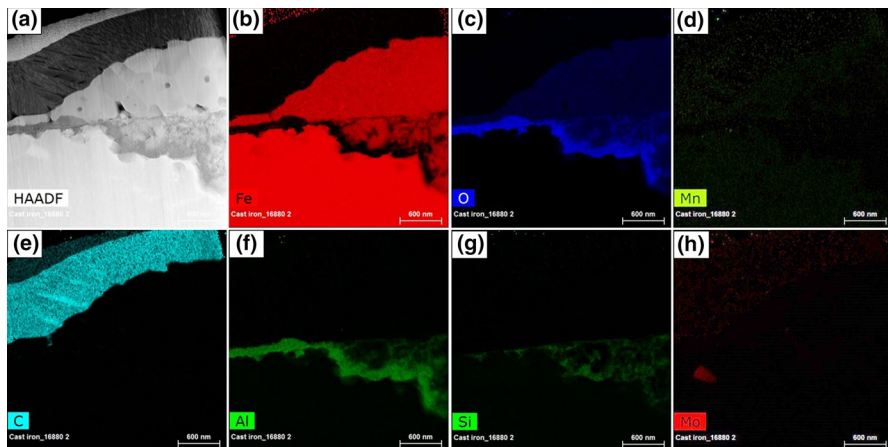


Fig. 8 STEM/EDS mapping of HSM3Al alloy oxidized in dry air at 800 °C for 50 h

or rapid growth of Fe-rich oxides [28]. That was probably why the chrome oxides were layered, as shown in Fig. 4. The synergetic effects of Al/Cr and Si were the primary reason for the improvement of the oxidation resistance.

Conclusion

Two new HiSiMo cast iron alloys have been developed for exhaust manifold applications by adding either 3wt.% Al or 1wt.% Cr. Alloy coupons were tested using cyclic oxidation (6 min cycles) in dry and wet air atmospheres at 800 °C. The reaction product microstructures were characterized after exposure to investigate the mechanism for the observed improvement in the oxidation resistance with the Cr and Al additions. The results showed that the introduction of Al or Cr created Al- or Cr-rich oxide layers, which substantially reduced the diffusion of oxygen, hence reducing the oxide thickness after these exposures.

Acknowledgements The authors would like to thank the financial support by the US Department of Energy, Office of Energy Efficiency and Renewable Energy (Vehicle Technologies Office, Propulsion Materials Program) under Award No. DE-EE0008458.

References

1. X. Wang, Y. Fan, X. Zhao, A. Du, R. Ma, and X. Cao, *Metals* 2019. <https://doi.org/10.3390/met9060648>.
2. D. Li, C. Sloss, and F. S. Amer, *Transactions of the American Foundry Society* **121**, 2013 (487).
3. D. Li and C. Sloss, *SAE International Journal of Materials and Manufacturing* **3**, 2010 (391).
4. S. Kim, S. Lee, K. Han, S. Hong, and C. Lee, *Metals and Materials International* **16**, 2010 (483). <https://doi.org/10.1007/s12540-010-0621-7>.
5. F. Tholence and M. Norell, *Oxidation of metals* **69**, 2008 (13).
6. K. Dawi, J. Favregeon, and G. Moulin, *Materials Science Forum* **595**, 2008 (743).

7. M. P. Brady, G. Muralidharan, D. N. Leonard, J. A. Haynes, R. G. Weldon, and R. D. England, *Oxidation of metals* **82**, 2014 (359).
8. M. Ekström, P. Szakalos, and S. Jonsson, *Oxidation of metals* **80**, 2013 (455).
9. K. H. Choe, S. M. Lee, and K. W. Lee, *Materials Science Forum* **654**, 2010 (542).
10. S. N. Lekakh, A. Bofah, R. Osei, R. O'Malley, L. Godlewski, and M. Li, *Oxidation of Metals* **95**, 2021 (251).
11. Y. Yang, Z. Cao, Z. Lian, and H. Yu, *Journal of Iron and Steel Research, International* **20**, 2013 (52).
12. D. Pierce, et al., *Progress in Materials Science* **103**, 2019 (109).
13. G. A. Celik, et al., *Journal of Mining and Metallurgy Section B: Metallurgy* **57**, (1), 2021 (53).
14. P. von Hartrott, T. Seifert, and S. Dropps, *SAE International Journal of Materials and Manufacturing* **7**, 2014 (439).
15. T. Seifert, R. Hazime, and S. Dropps, *SAE International Journal of Materials and Manufacturing* **7**, 2014 (421).
16. H. Guo, W. Jia, and F. Ahdad, "Modeling and Simulation of Tube with HiSiMo Ductile Iron under High Speed Impact," SAE Technical Paper, 2018.
17. S. N. Lekakh, A. Bofah, W.-T. Chen, L. Godlewski, and M. Li, *Metallurgical and Materials Transactions B* **51**, 2020 (2542). <https://doi.org/10.1007/s11663-020-01975-w>.
18. B. A. Pint, P. F. Tortorelli, and I. G. Wright, *Oxidation of Metals* **58**, 2002 (73).
19. B. A. Pint, J. A. Haynes, and B. L. Armstrong, *Surface and Coatings Technology* **215**, 2013 (90).
20. B. A. Pint, *OXIDATION OF METALS* **95**, 2021 (335).
21. F. Tholence and M. Norell, *Oxid Met* **69**, 2008 (13). <https://doi.org/10.1007/s11085-007-9081-y>.
22. M. Hasegawa, "Chapter 3.3 - Ellingham Diagram," in *Treatise on Process Metallurgy*, ed. S. Seetharaman, (Boston: Elsevier, 2014), pp. 507–516. <https://doi.org/10.1016/B978-0-08-096986-2.00032-1>.
23. I. G. Wright and R. B. Dooley, *Materials at High Temperatures* **30**, 2013 (168).
24. M. P. Brady, D. N. Leonard, J. R. Keiser, E. Cakmak, and L. E. Whitmer, *Corrosion* **75**, 2019 (1136).
25. G. C. Wood and D. P. Whittle, *Corrosion Science* **7**, 1967 (763).
26. J. Paidassi, *Revue de Métallurgie* **54**, 1957 (569).
27. P. Novák and K. Nová, *Materials* 2019. <https://doi.org/10.3390/ma12111748>.
28. R. N. Durham, B. Gleeson, and D. J. Young, *Oxidation of Metals* **50**, 1998 (139). <https://doi.org/10.1023/A:1018880019395>.

Publisher's Note Springer Nature remains neutral with regard to jurisdictional claims in published maps and institutional affiliations.